Medical Image Analysis 57 (2019) 56–71

Contents lists available at ScienceDirect

Medical Image Analysis

journal homepage: www.elsevier.com/locate/media

Influence of coupled hemodynamics-arterial wall interaction on compliance in a realistic pulmonary artery with variable intravascular wall properties

Ullhas U. Hebbar, Rupak K. Banerjee*

593 Rhodes Hall, Department of Mechanical Engineering, University of Cincinnati, OH, 45221, United States

ARTICLE INFO

Article history:
Received 17 December 2018
Revised 1 May 2019
Accepted 19 June 2019
Available online 21 June 2019

Keywords:
Cardiac MRI
Pulmonary hypertension
Artery wall pre-stress
Cardiovascular FSI

ABSTRACT

Pulmonary hypertension is characterized by elevation of pulmonary artery (PA) pressure (p) and structural remodeling of the PA wall, leading to reduction in arterial compliance (c). As a step towards improving diagnosis of pulmonary disease, we use the PA branch geometry (main pulmonary artery (MPA) branching into left (LPA) and right (RPA) pulmonary arteries) obtained from MRI in conjunction with an inverse algorithm to obtain the pre-stress level in the artery walls. Next, a coupled blood–wall interaction (BWI) calculation provides hemodynamic information as well as compliance of the PA walls. We show that the computed load-free geometry from the inverse algorithm exhibits a 27.8% lower inner diameter (d) and 18.5% lower outer d compared to the *in vivo* geometry from MRI. Further, the mean p computed from the BWI computation in the main PA (p_{MPA-n}) is within 4% of the mean p_{MPA-e} (n-numerical; e-experimental). Also, the mean Q computed in the left PA (Q_{LPA-n}) is within 10% of the mean Q_{LPA-e}. Finally, the compliance c_{MPA-n} is computed to be 27% lower than c_{MPA-e}, while the c_{LPA-n} is computed to be 20.4% lower than c_{LPA-e}. Importantly, the PA shows significant intra-vascular variation in compliance, with the MPA showing higher overall compliance compared to the LPA (3.5–4 times).

Published by Elsevier B.V.

1. Introduction

Arterial wall compliance is an important aspect of the human circulatory system that influences structural parameters such as stress and strain, as well as hemodynamic parameters such as transient pressure drop and flow rate. Structural remodeling of the pulmonary artery (PA) wall and consequent reduction in arterial compliance is often associated with pulmonary hypertension (PH), and if left untreated, PH can result in right heart failure and subsequent death. Computational methods can aid in evaluating the role of hemodynamics in vascular disease pathogenesis, as well as evaluating healthy or diseased vascular compliance by analyzing the coupled interaction between blood flow and the arterial wall. Important factors that influence compliance are the wall pre-stress, the artery material property, and the physiological pressure, all of which have been incorporated in the current numerical study.

PA structural remodeling and disease progression. Pulmonary hypertension (PH) is a disease characterized by elevated pulmonary arterial pressure and is associated with reduced arterial compliance and structural remodeling. While the etiology of PH remains uncertain, all forms of PH are associated with vasoconstriction and, in the long-term, result in right ventricular hypertrophy (Crosswhite and Sun, 2014; Shimoda and Laurie, 2013). Vascular remodeling of the pulmonary arteries in PH is characterized by thickening of the intimal/medial layer of the arteries as well as smooth muscle cell proliferation, which results in reduction of lumen cross-sectional areas and increased right ventricular afterloads. Huang et al. (2001a) have reported changes in mechanical properties of the pulmonary arteries in a rat when subjected to hypoxic breathing, which emulates the vascular remodeling seen in PH. Increased pulmonary vascular resistance and right ventricular enlargement has been observed in adults residing in high-altitude environments, and importantly, the post-mortem studies have shown medial hypertrophy and smooth muscle proliferation (Canepa et al., 1956). Coupled computational analyses of patient-specific arterial geometries with appropriate material properties of the artery can provide realistic compliance and pressure drop information to potentially assist the diagnosis of PH and associated conditions in future.

1.1. Evaluation of pre-stress in arterial walls

PA wall pre-stress. In the *in vivo* condition, the human artery is in a pre-stressed configuration primarily attributed to the *in*

* Corresponding author.
E-mail address: rupak.banerjee@uc.edu (R.K. Banerjee).

https://doi.org/10.1016/j.media.2019.06.008
1361-8415/Published by Elsevier B.V.

vivo lumen pressure in conjunction with the effect of tethering due to surrounding tissue (adventitia) (Holzapfel and Ogden, 2014). A manifestation of this pre-stress is the axial and radial contraction observed when artery tissue is excised from the body (Holzapfel and Ogden, 2014), which is also referred to as the load-free state of the artery. For example, axial stretches of 15% to 70% from the excised lengths have been suggested for mammalian pulmonary artery segments (Huang et al., 2001b; Debes and Fung, 1995). Physiologically, arteries in the body exhibit a time-averaged pre-stress that is in static equilibrium with the mean lumen pressure and *in vivo* axial stretch. However, this pre-stress cannot be measured using imaging techniques and thus reconstructed patient specific arterial geometries obtained from imaging modalities are stress-free. In order to obtain realistic patient-specific compliance and hemodynamics, the arterial wall pre-stress needs to be accounted for in the computational formulation using the load-free state of the artery.

Several methods have been proposed to compute the load-free arterial configuration and the pre-stress using computational techniques. These include manual trial-and-error techniques as well as automatic inverse techniques such as solving the inverse elastostatics problem, or shape matching techniques.

Trial-and-error methods. Tang et al. (2005) and Huang et al. (2009) have employed a manual trial-and-error technique to obtain load-free arterial geometries from imaging data for coronary and carotid arteries. Roy et al. (2008) and Konala et al. (2011) have also reported a similar technique for idealized canine femoral arteries and stenosed human coronary arteries. Although these techniques are suitable for idealized axisymmetric geometries, they are not suitable for complex patient-specific geometries with variable wall thickness and non-circular arterial cross-sections.

Inverse methods. Another class of techniques to compute load-free geometries are classified as automatic inverse methods. Putter et al. (2007) and Gee et al. (2009) have proposed a method utilizing a Lagrangian formulation wherein lumen pressure has been increased incrementally while updating the deformation gradient to maintain static equilibrium. The inverse elastostatics problem has also been solved by Govindjee et al. (1996) and Lu et al. (2007) to obtain load-free artery geometries. A recent study by Vavourakis et al. (2016) has used a generalized pressure–displacement formulation to obtain load-free states of incompressible biological tissue. It may be noted that the above studies require custom finite element (FE) solvers with specialized formulations.

On the other hand, shape matching inverse techniques utilize either an iterative backward displacement technique, or an optimization-based algorithm to obtain load-free geometries which resemble the *in vivo* arterial geometry when the physiological loads are applied. These techniques can employ FE solvers with minimal scripting and customization to obtain load-free geometries. Raghavan et al. (2006) have developed a technique for abdominal aortic aneurysms which has utilized a backward displacement computation in the first iteration and single-parameter optimization in the subsequent iterations to obtain load-free geometries. Bols et al. (2013) have used backward displacement iterations to predict the load-free state and pre-stress for a complex mouse abdominal aorta model with branching. However, it may be noted that these studies have only used the lumen pressure as an input to the algorithm, while neglecting the axial stretch. Recent studies by Das et al. (2015a) and Banerjee et al. (2017) have successfully implemented an optimization based inverse algorithm for circular and tapered arterial geometries which have included the *in vivo* axial stretch as well as non-linear hyperelastic material models. However, this approach requires advancement of methodology for 3D non-circular patient-specific geometries.

PA wall compliance. The large arteries, including the aorta and pulmonary arteries exhibit rapid dilation and contraction during systole and diastole, respectively. Studies by Jin et al. (2003) and Borgen et al. (1989) have reported diameter variations of 11% and 9.5% over the cardiac cycle for the pulmonary artery and the ascending aorta, respectively. Megerman et al. (1986) have documented diameter variations of 0.3% to 0.07% per mmHg over the cardiac cycle for a canine femoral artery. Finally, Borges et al. (1997) have performed a study on the pulmonary arteries of normal and hypertensive adults to study the feasibility of intravascular ultrasound techniques. Internal area changes of 7.5% have been observed over the cardiac cycle in the healthy volunteers. In summary, compliance of the arterial walls has a significant effect on the pressure drop, flow rate through the vessel as well as the vessel impedance. Therefore, improved determination of compliance in numerical methodologies is necessary to obtain physiological results for arterial stress–strain as well as hemodynamic measures.

1.2. Significance and novelty

The current numerical study with 3D patient-specific arterial geometry is *significant as it can potentially assist in better diagnosis of pulmonary vasculature disorders in future, while predicting the prognosis of pulmonary disease.* Although several computational studies have been performed to evaluate the pressure-flow hemodynamics and structural stress–strain measures of systemic and coronary vasculature using coupled blood–wall interaction (BWI), there have been relatively few studies related to the pulmonary arteries. Hunter et al. (2006) analyzed the pediatric pulmonary circuit to study congenital heart disease, but the wall pre-stress was not considered. Das et al. (2011, 2015a) have developed energy-based indices for pulmonary insufficiency diagnosis using patient-specific computational models, but a rigid artery wall assumption has been used. Finally, Long et al. (2012) studied hemodynamic conditions in a Fontan procedure but used linear elastic material properties, while it is known that pulmonary vasculature deformation is generally hyperelastic as well as non-isotropic. *Therefore, the BWI computation in this study is novel as it incorporates the wall pre-stress from an inverse algorithm using hyperelastic, orthotropic material properties in a realistic 3D PA geometry. Further, close agreement is observed between the computed compliance and pressure-flow hemodynamics with the corresponding experimental values.*

Summarizing the important aspects of this research – the previously developed optimization-based inverse algorithm has been modified with a backward displacement approach. Subsequently, load-free and pre-stressed geometries are generated with the mean lumen pressure and *in vivo* axial stretch as inputs to the algorithm. The inverse algorithm is implemented for a complex 3D patient-specific PA branch with non-circular geometry and varying wall thickness. In order to test the accuracy of the modified inverse algorithm, the specific aims of the study are: (a) obtain the load-free and pre-stressed conditions for a 3D complex patient-specific PA branch with artery-specific material properties; (b) evaluate the pressure-flow hemodynamics within the pre-stressed PA branch using a coupled blood–wall interaction (BWI) analysis and compare it with clinical data; (c) compare arterial wall compliance calculated from a numerical method with measurements under clinical conditions, and determine the difference in compliance between the main and branched PA's.

2. Methods

The methodology is composed of three steps: (1) develop patient-specific material models for the PA wall using pressure-diameter data available from cardiac catheterization and phase

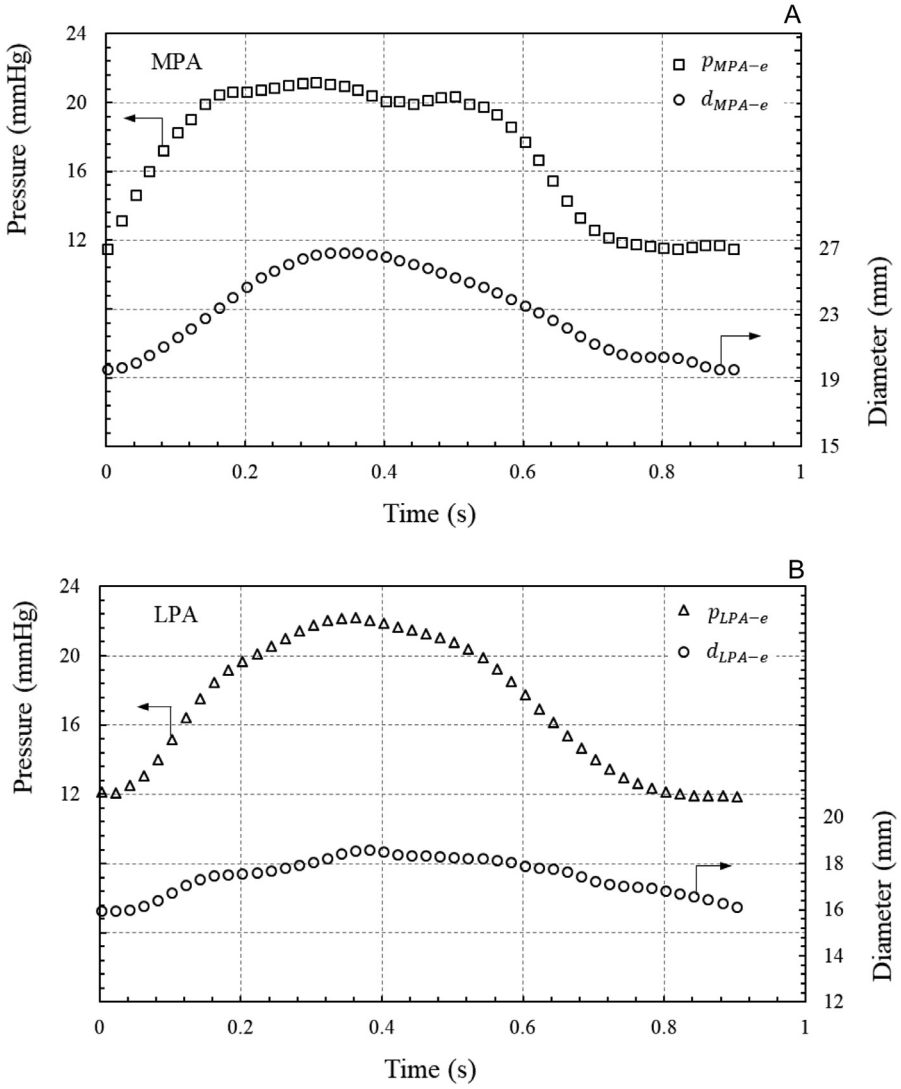

Fig. 1. (A) Pressure (from cardiac catheterization) and diameter (from PC-MRI) for the MPA over time measured under clinical settings. (B) Pressure and diameter for the LPA over time measured under clinical settings.

contrast MRI (PC-MRI) techniques; (2) implement a shape matching inverse algorithm to compute the load-free geometry and obtain the arterial wall pre-stress exposed to *in vivo* pressure and axial stretch for a 3D patient-specific PA geometry; (3) and obtain numerical pressure-flow hemodynamic data and determine compliance of the PA walls using a coupled blood–wall interaction (BWI) computation.

2.1. Patient-specific artery wall material properties

Patient characteristics. The PA geometry and patient specific clinical data has been obtained from previously conducted studies by our group (Das et al., 2011, 2015a) for a single pediatric patient (Age: 14 years; Sex: male; Weight: 55 kg; BSA: 1.57 m^2; Pulse cycle: 0.9 s) with normal right-ventricle physiology and a functioning pulmonary valve. MRI and cardiac catheterization have been performed on the subject for assessing the status of the left heart. Flow rate and diameter measurements have been made for all the three PA branches (MPA, LPA and RPA). However, pressure has been recorded for the MPA and LPA only. All study protocols have been approved by the Institutional Review Board at the Cincinnati Children's Hospital and Medical Center.

Pressure and diameter measurements. Pressure (p) and diameter (d) measurements for the PA are made using cardiac catheterization and PC-MRI techniques, respectively. Fig. 1(A) plots the MPA pressure (p_{MPA-e}) and diameter (d_{MPA-e}) with respect to time. The p_{MPA-e} profile shows a peak systolic pressure of 21.3 mmHg at 0.3 s, and there is a distinct dicrotic notch observed at 0.42 s, which represents the closing of the pulmonary valve. The d_{MPA-e} varies from 19.79 mm at end diastole to 26.86 mm at peak systole (0.34 s). The time difference of 0.04 s between the p_{MPA-e} and d_{MPA-e} peaks could be a result of either arterial wall viscoelasticity or the pressure and diameter measurements being done at different, but nearby locations.

On a similar note, Fig. 1(B) plots the LPA pressure (p_{LPA-e}) and diameter (d_{LPA-e}) with respect to time. The pulsatile p_{LPA-e} profile shows a peak systolic pressure of 22.3 mmHg at 0.36 s, with no distinct dicrotic notch. The d_{LPA-e} varies from 16.18 mm at end diastole to 18.66 mm at peak systole, measured at 0.38 s. Again, a time difference of 0.02 s is observed between the p_{LPA-e} and d_{LPA-e} peaks. It may be noted that both the p_{MPA-e} and p_{LPA-e} show very similar cycle averages of 17.2 mmHg, which is used as an input to the inverse algorithm implemented later in the study.

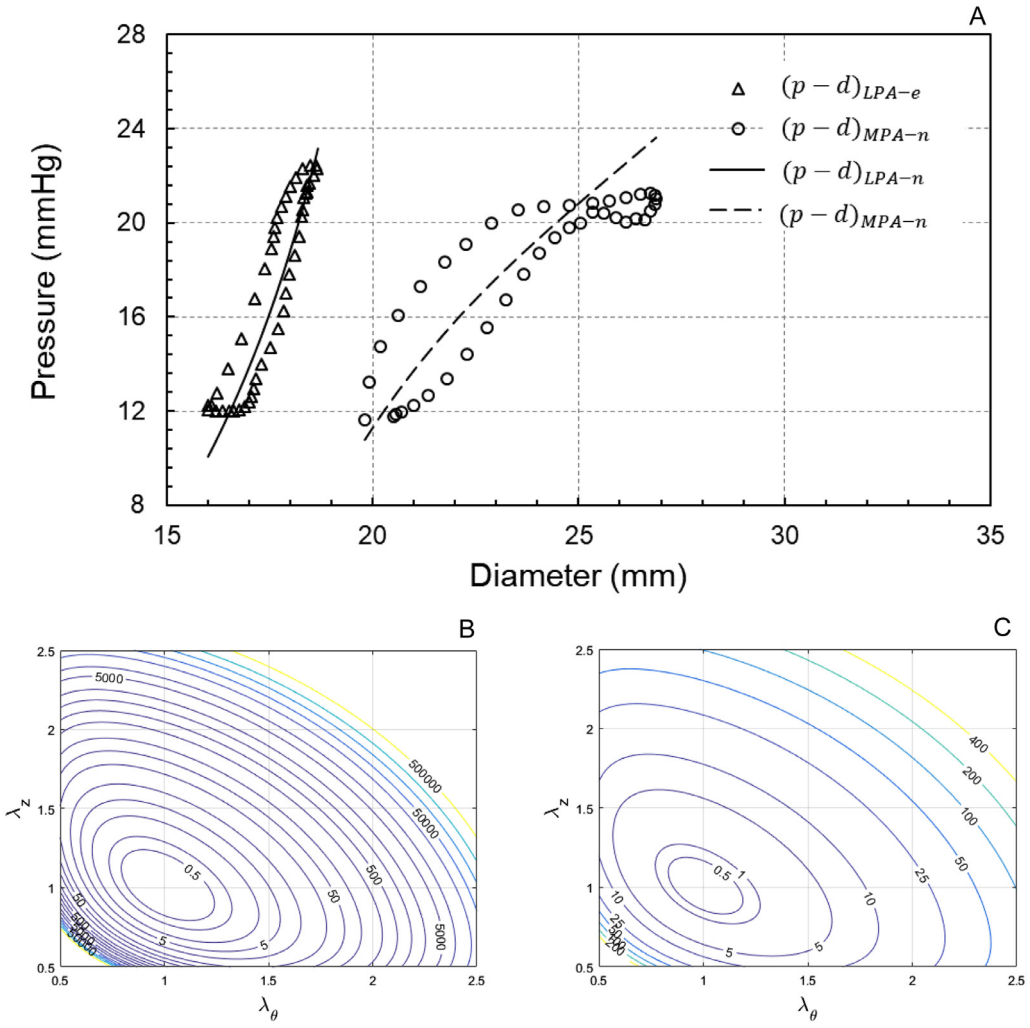

Fig. 2. (A) Pressure vs. diameter obtained from patient data for the MPA and LPA, with numerical curve-fits for the pressure-diameter relationship. (B) Strain energy potential (SEP) plotted with respect to axial and circumferential stretch ratios for the LPA. (C) SEP plotted with respect to axial and circumferential stretch ratios for the MPA.

Artery-specific material models from pressure–diameter relationships. Fig. 2(A) shows the pressure plotted with respect to diameter $(p-d)$ measured under clinical conditions. Separate material models are developed for the MPA and LPA, as the $p-d$ variations indicate distinct wall properties. It is important to note that a separate material model has not been developed for the RPA, as p has not been recorded for this branch. Instead, the LPA material model is assigned to the RPA branch. In this study, the hyperelastic modified Mooney–Rivlin material model is used to represent the MPA and LPA walls, for which the strain energy potential (SEP) is given by:

$$W = c_1(I_1-3) + D_1\left(e^{D_2(I_1-3)}-1\right) + 2\frac{k_1}{2k_2}\left[e^{k_2(I_4-1)^2}-1\right] \qquad (1)$$

where, c_1, D_1, D_2, k_1 and k_2 are unknown model constants; I_1 and I_4 are invariants expressed as a function of stretch ratios in the axial (λ_z) and circumferential (λ_θ) directions. Here, the stretch ratio is defined as the ratio of deformed length to undeformed length in the characteristic direction.

In order to obtain the unknown model constants and the *in vivo* λ_z used later in the study, a non-linear least-squares optimization technique developed by D'Souza et al. (2017) of our research group has been utilized. In brief:

Table 1
PA material model constants obtained from the non-linear optimization technique developed by D'Souza et al. (2017).

	δ_{IV}	c_1 (kPa)	D_1 (kPa)	D_2	k_1 (kPa)	k_2
MPA	1.03	3.35	2.14	0.7	0.	0
LPA	1.04	0.43	0.89	2.61	0.54	0.3

a) The p and d values from the clinical data are used to estimate experimental stresses (σ_{exp}) for the LPA and MPA under the thin-walled cylinder assumption.
b) Theoretical expressions for the stresses (σ_{th}) are obtained from the Mooney–Rivlin SEP and are expressed as functions of the unknown model constants and λ_z.
c) The Levenberg–Marquardt minimization technique is then used to compute the set of model constants and λ_z which minimizes the difference between σ_{exp} and σ_{th}.

The model constants obtained for the MPA and LPA have been reported in Table 1. It may be noted that the λ_z is also referred to as δ_{IV} in the subsequent sections in order to simplify the nomenclature.

Fig. 2(A) also shows the predicted material models for the MPA and LPA, which are obtained from the least-squares optimization

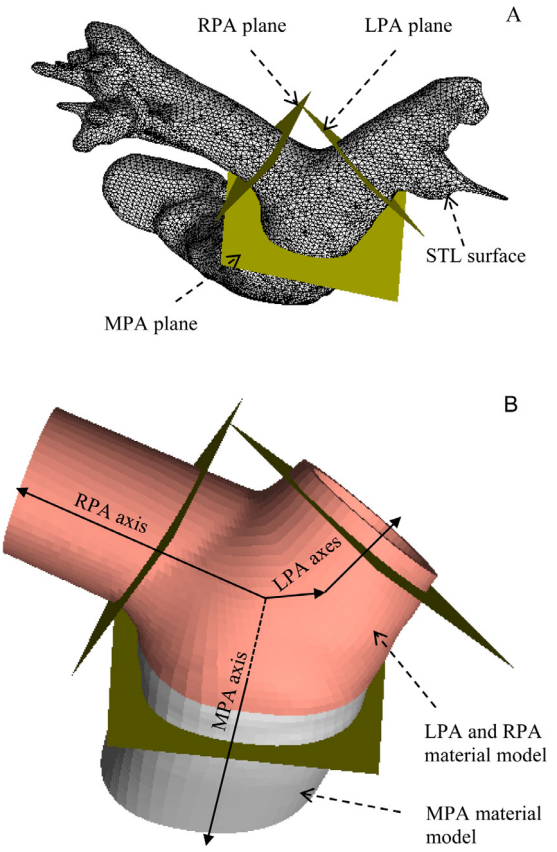

Fig. 3. (A) Faceted geometry obtained from Cardiac MRI, with phase-contrast MRI (PC-MRI) planes indicated. (B) Segmented geometry with different material models and co-ordinate system axes.

technique. The predicted $p-d$ relationship for the LPA closely follows the experimental data over the entire $p-d$ range, while the relationship for the MPA closely follows the experimental data until a d value of 25 mm. It may be noted that data points beyond 25 mm in the MPA $p-d$ relationship have been truncated during the least-squares optimization implementation. This is done to ensure physiologically relevant wall deformation and numerical stability. Further clarification is provided in the discussion section.

Fig. 2(B) and (C) show the SEP contour with respect to the axial (λ_z) and circumferential (λ_θ) ratios for the MPA and LPA, respectively. Importantly, the potentials for both the MPA and LPA show convexity, an important feature for numerical stability and realistic material response (D'Souza et al., 2017). Also, the SEP values for both the MPA and LPA are 0.0 for $\lambda_z = 1.0$ and $\lambda_\theta = 1.0$, indicating zero potential at no stretch.

2.2. Determination of pre-stress in arterial walls

PA geometry reconstruction. Fig. 3(A) shows the faceted stereolithographic (STL) surface of the PA inner wall. The indicated PC-MRI planes show the locations where flow rate (Q) and d variations have been measured for the PA. The faceted inner surface is first truncated and smoothed to form the PA computational domain. This is done to remove MRI artifacts and ensure realistic representation of the PA geometry. Previous clinical research (Hunter et al., 2006) has reported that the PA wall thickness is approximately 10% of the lumen diameter. Accordingly, the inner surface is offset by 10% of the diameter to create the outer surface of the PA. Finally, surfaces are included at the ends of the arteries to obtain the final computational geometry shown in Fig. 3(B). The two shades in the figure represent the different material models used for the MPA and the branched arteries (LPA and RPA). Geometry operations including segmentation, smoothing and lofting of the surfaces are performed using a pre-processor (ICEM CFD 18.0, ANSYS Inc.).

Further, different co-ordinate systems are used for the MPA, LPA and RPA segments, as indicated in Fig. 3(B). These systems define the axial and circumferential directions for the different segments of the PA geometry. It is worth noting that the LPA has been split into two segments, and each segment is assigned a different co-ordinate system to better account for the abrupt change in direction from the LPA to the RPA. Different materials and co-ordinate systems are used in this study to ensure physiologically realistic deformations of the artery and better measures for wall pre-stress.

Governing equation. The inverse algorithm described in the following section uses a forward finite element (FE) formulation, which satisfies the following stress equilibrium condition:

$$\sigma^s_{lm,l} = 0, \;\; l, m = 1, 2, 3 \tag{2}$$

where σ^s is the Cauchy stress tensor for the PA wall. Eq. (2) represents the static equilibrium of the arterial wall with the *in vivo* loads.

Constraints and boundary conditions. The displacement of the end surface nodes of the MPA and LPA are constrained to be equal to the *in vivo* axial stretches (δ_{IV}) from Table 1. Since a separate material model is not developed for the RPA, the nodes on the RPA end surface are assigned the same δ_{IV} as the LPA. In order to prevent non-physiological twisting or free body motion of the arteries during the computation, the centerline of the PA geometry is also constrained by restricting the tangential degree of freedom for all arterial segments. However, the radial motion of the artery wall is allowed. Finally, incompressibility is enforced in the FE model using a pressure–displacement mixed interpolation scheme.

Discretization. The segmented PA geometry is first divided into sub-domains, and a structured meshing algorithm is utilized to generate an 8-node hexahedral mesh composed of 16,268 elements and the thickness of the PA wall is modeled using 5 uniformly spaced nodes in the radial direction. Again, the structured mesh is generated using the same pre-processor (ICEM CFD 18.0, ANSYS Inc.).

Shape matching inverse algorithm. The inverse algorithm of this study has adapted a combination of methods developed by Das et al. (2015b) and Banerjee et al. (2017) of our research group, as well as Bols et al. (2013), with some modifications that are discussed below. The previously developed inverse algorithm by our group (Das et al., 2015b; Banerjee et al., 2017) consists of a shrink operation which applies a fixed reduction in the axial and radial directions. This is followed by a fit operation, which applies the *in vivo* pressure and axial stretch. These shrink and fit operators used a frictionless, rigid contact surface surrounding the PA geometry for obtaining the pre-stressed arterial geometry. However, for the current method, such an approach was not adopted. Furthermore, the shrink operator for the previous method used an optimization based technique to determine the axial and radial reductions. In contrast, a backward displacement method proposed by Bols et al. (2013) is implemented for the current method.

In line with our earlier studies (Das et al., 2015a,b; Banerjee et al., 2017), the modified algorithm consists of two operators as discussed above. The fit operator (F) applies the *in vivo* loads in sequence: 1) axial stretch (δ_{IV}) and 2) mean pressure (P_{IV}), while the shrink operator (S) reduces the axial and radial dimensions of the PA, providing a new load-free geometry. Fig. 4 illustrates the sequence of operations that is further discussed below.

The inputs to the algorithm are the *in vivo* PA geometry [$A(x_{IV}, 0)$], which is a cycle average of the PA geometry obtained from Cardiac MRI, and the *in vivo* loads: P_{IV} and δ_{IV}. The notation $A(x_{IV}, 0)$ indicates the artery configuration with the first term in the parenthesis being the vector of nodal positions, and the second term

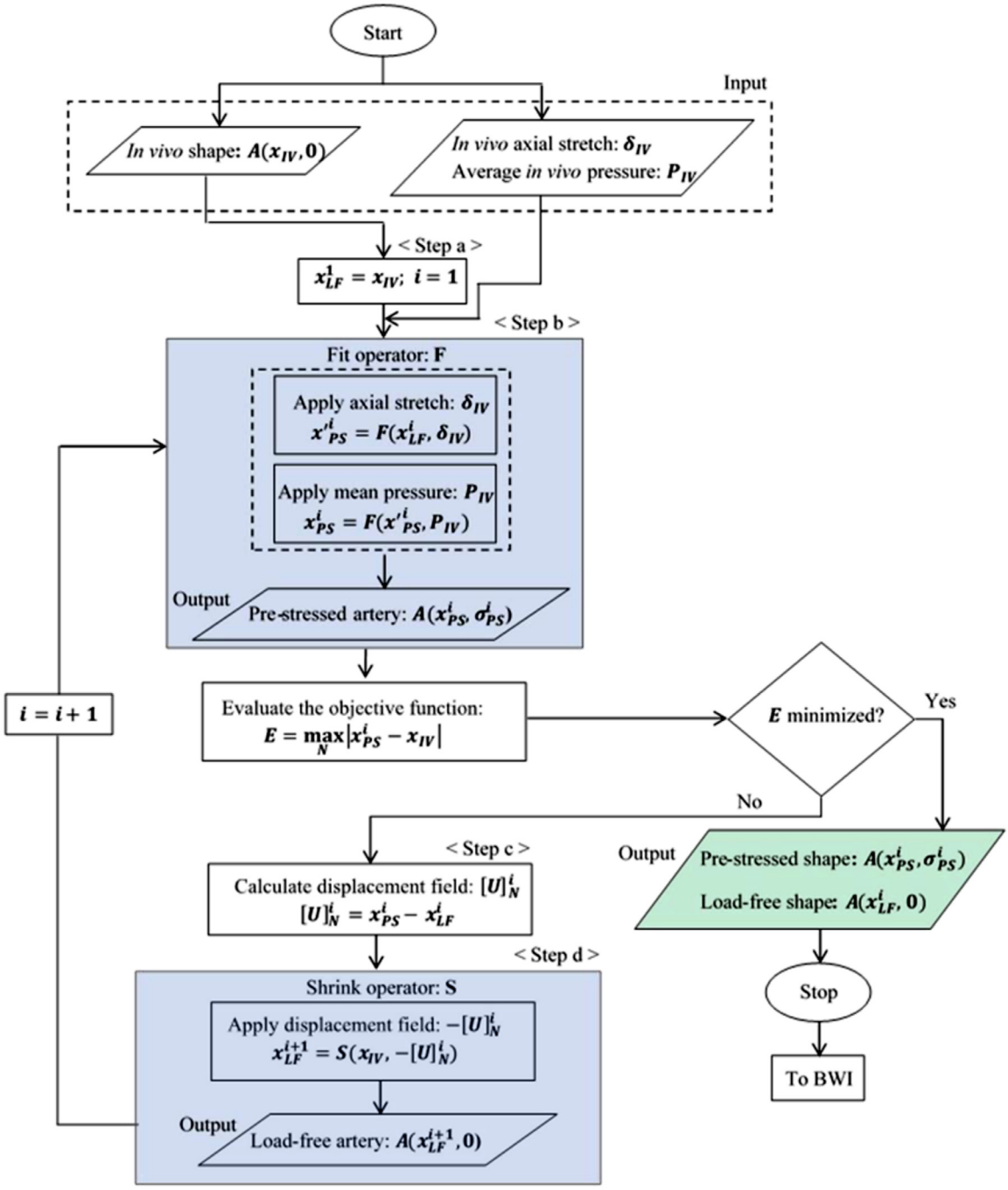

Fig. 4. Flowchart summarizing the shape matching algorithm used to estimate the pre-stress in the PA wall.

representing the stress in the artery wall. Also, the subscript '*IV*' indicates *in vivo*. The P_{IV} is determined as the time-averaged pressures in the MPA and LPA and is considered to be 17.2 mmHg. The *in vivo* δ_{IV} for the MPA, LPA and RPA are obtained as outputs from the non-linear least squares optimization (Table 1).

Below is a sequential implementation of the iterative inverse algorithm for $i = 1, 2, \ldots, n$

a) First, the *in vivo* geometry $[A(x_{IV}, 0)]$ is taken as an *initial* guess ($i = 1$) for the load-free PA geometry $[A(x^1_{LF}, 0)]$. Here, subscript '*LF*' indicates load-free.
b) Next, the fit operator F applies the *in vivo* loads in sequence: 1) δ_{IV}; followed by 2) P_{IV}, on the $A(x^1_{LF}, 0)$ using a forward FE calculation to obtain the first pre-stressed geometry $[A(x^1_{PS}, \sigma^1_{PS})]$. Here, subscript '*PS*' indicates pre-stressed.
c) The nodal displacement field ($[U]^1_N$) is then computed by subtracting x^1_{LF} from x^1_{PS}. Generally, it is worth noting that $[U]^i_N$ includes both axial and radial displacements and is always positive since $x^i_{PS} > x^i_{LF}$. Here, the subscript '*N*' represents the set of nodes of the solid mesh and superscript '*i*' the iteration number.
d) The nodal displacement field is then applied as a backward displacement ($-[U]^1_N$) to $A(x_{IV}, 0)$ to obtain a new guess for the load-free geometry $[A(x^2_{LF}, 0)]$.
e) Again, the fit operator F applies the *in vivo* loads in sequence: 1) δ_{IV}; followed by 2) P_{IV}, on the $A(x^2_{LF}, 0)$ using a

forward FE calculation to obtain the second pre-stressed geometry $[A(x^2_{PS}, \sigma^2_{PS})]$.

f) The objective function E, expressed as the maximum of the difference between nodal positions of the pre-stressed and *in vivo* geometries $[E = \max_N |x_{PS} - x_{IV}|]$, is then computed. If the condition $[E < 0.1\,mm]$ is satisfied, then the algorithm is terminated and the $A(x^2_{LF}, 0)$ and $A(x^2_{PS}, \sigma^2_{PS})$ are stored.

g) If the function E is not satisfied, the nodal displacement field $([U]^2_N)$ is then computed by subtracting x^2_{LF} from x^2_{PS}, and is applied to the $A(x_{IV}, 0)$ as a backward displacement to generate $A(x^3_{LF}, 0)$.

h) Steps e) to g) are repeated until the condition $E < 0.1$ is satisfied.

i) The outputs from the inverse algorithm are the final $A(x^i_{LF}, 0)$ and the final $A(x^i_{PS}, \sigma^i_{PS})$ containing the computed pre-stress in the PA wall.

It may be noted that for the first iteration, the evaluation of E and the check for minimization are skipped. Step a) to step d) have been marked in the flowchart (Fig. 4) for clarification. The forward FE computations are performed using an FE solver (ABAQUS 6.14-2, Dassault systems), while the steps of the inverse algorithm are implemented using the Python programming language (Python 3.5, Python Software Foundation).

2.3. Determination of PA wall compliance and pressure-flow hemodynamics using blood–wall interaction (BWI)

Artery geometry. The load-free PA geometry $[A(x_{LF}, 0)]$ obtained from the inverse algorithm is used as the initial geometry for the numerical BWI calculation. It is worth noting that a 3D BWI calculation for a patient-specific arterial geometry with artery specific material models is performed using the following set of equations.

Governing equations. The governing equations for blood flow are:

$$\nabla \cdot u = 0 \quad \text{(Continuity equation)} \tag{3}$$

$$\rho\left(\frac{\partial u}{\partial t} + ((u - u_g)\cdot\nabla)u\right) = -\nabla p + \mu\nabla^2 u \quad \text{(Momentum equation for blood flow)} \tag{4}$$

where ρ is the density of blood ($1050\,kg/m^3$), u and p are the velocity and pressure fields, u_g is the mesh velocity of the fluid domain and μ is the dynamic viscosity of blood.

The governing equation for arterial wall mechanics is:

$$\rho^s v_{l,tt} = \sigma^s_{lm,m} \quad \text{where l, m} = 1, 2, 3;\ \text{sum over m} \tag{5}$$

where ρ^s is the density of the artery wall ($1000\,kg/m^3$), v is the solid nodal displacement, subscript 't' indicates the time derivative and σ^s is the Cauchy stress tensor for the artery wall.

Boundary conditions and solution initialization. Similar to the forward FE calculation used in the inverse algorithm implementation, the displacement of the ends of the three artery branches (MPA, LPA and RPA) are constrained to be equal to the *in vivo* δ_{IV}. Again, the centerline of the PA geometry is held fixed by restricting the tangential degree of freedom. This avoids non-physiological motion (twisting or solid-body rotation) of the PA.

For the fluid domain, the MPA and RPA boundaries are assigned velocity boundary condition (BC's), while the LPA boundary is assigned a normal traction BC. Although the computational domain extended beyond the locations of the PC-MRI planes for the MPA and RPA, the phase difference between the measured velocity profiles at the PC-MRI plane and the extended boundary is neglected due to the short distance (under 14 mm) between these locations. The normal traction BC at the LPA boundary is also set equal to the measured p_{LPA-e} as the distance between the boundary and the PC-MRI plane is relatively small (under 5 mm). Importantly, the variations of lumen area and therefore, the velocity obtained from numerical calculations over the pulse cycle may differ from the experimental data. Therefore, the velocity BC's applied at the MPA and RPA boundaries are back calculated such that they are the same as the measured flow rates (Fig. 5(A)) at the PC-MRI measurement planes. To accomplish this, an iterative procedure similar to the one used by Roy et al. (2008) from our research group is implemented.

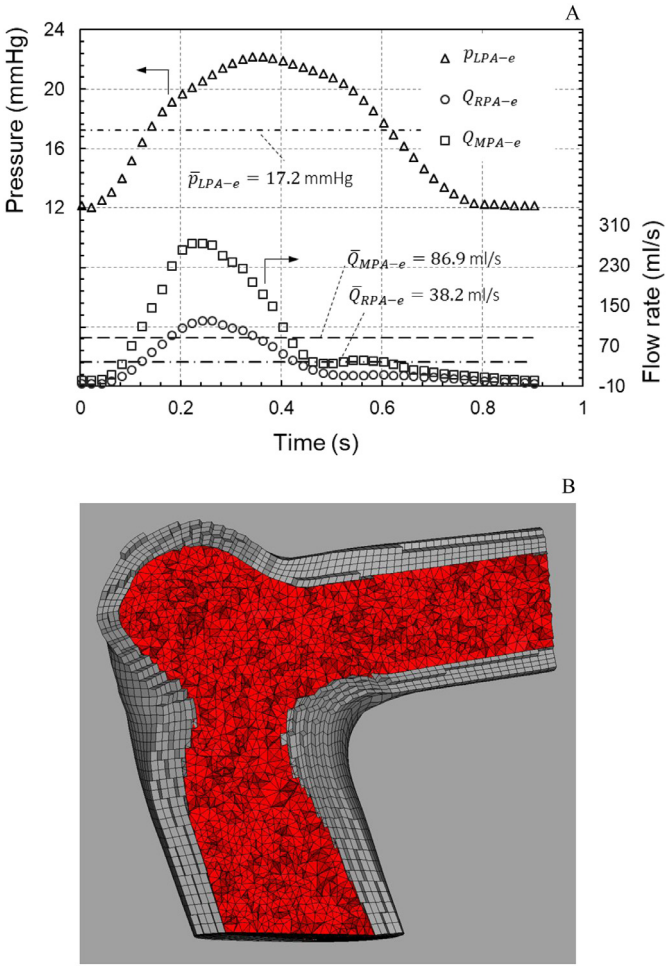

Fig. 5. (A) Measurements under clinical conditions used to compute patient-specific boundary conditions (BC's). (B) Cut-section view of the fluid and solid mesh for the BWI computation.

From Fig. 5(A), the peak systolic p_{LPA-e} is measured to be 22.3 mmHg, and unlike the p_{MPA-e}, there is no distinct dicrotic notch observed. As mentioned earlier, the mean pressure $\bar{p}_{LPA-e}$ is measured to be 17.2 mmHg. The MPA flow rate (Q_{MPA-e}) shows a systolic peak of 277.3 ml/s, while the peak systolic Q_{RPA-e} is 124.4 ml/s. Also, the Q_{RPA-e} shows reverse flow during end-diastole. Finally, the mean MPA flow rate ($\bar{Q}_{MPA-e}$) is measured to be 86.9 ml/s, while the $\bar{Q}_{RPA-e}$ is 38.2 ml/s.

Since the BWI calculation obtains the arterial pressure-flow hemodynamics by computing the coupled interaction between the blood and PA wall, a separate set of BC's are required at the blood–wall interface:

$$\sigma^s_{lm}.n_m = 0 \quad \text{(outer wall assumption)} \tag{6}$$

$$\sigma^s_{lm}.n_m = \sigma^f_{lm}.n_m \quad \text{(blood} - \text{wall interface stress compatibility)} \tag{7}$$

$$v^s = v^f \quad \text{(blood} - \text{wall interface displacement compatibility)} \tag{8}$$

where n_m is the normal vector to the element face, σ^f_{lm} is the Cauchy stress tensor for the fluid and v^f is the nodal displacement for the fluid domain. Although under *in vivo* conditions the outer wall of the artery is attached to adventitial tissue, Eq. (6) is used as an outer wall assumption since adventitial tissue surrounding the artery wall is not modeled in this study.

Starting with the $A(x_{LF}, 0)$, and initial zero values for the pressure and velocity throughout the domain, a steady state calculation is first used to increase the p and u field to a physiologic average value which is used as a starting or initial condition ($t = 0$) for the pulsatile calculation. Uniform increments of 10 load-steps have been used for the steady-state calculation, leading to pre-stressing and deformation of the artery wall. Finally, the coupled interaction between the deformable artery wall and pulsatile blood flow is calculated for 3 pulse cycles to ensure convergence.

Discretization. Fig. 5(B) shows a cut-section view of the fluid and solid meshes used for the BWI calculation. The mesh is composed of 16,268 8-node hexahedral elements for the solid domain with 5 nodes across the thickness of the PA wall in the radial direction, and 139,243 4-node tetrahedral elements for the fluid domain. Steered adaptive meshing (Bathe et al., 2009) is also used during the steady state calculation to update the fluid mesh at the 3rd and 7th load increment to avoid excessive mesh distortion as in the case of an artery. In order to ascertain mesh convergence, a numerical calculation is performed using a refined mesh composed of 330,124 tetrahedral elements. The number of solid elements is not altered as the mesh in the radial direction is determined to be of adequate quality.

Material properties. The PA wall is assigned the same material property as the one used for the inverse algorithm. A non-Newtonian Carreau model is used to model the blood flow. The shear rate dependent viscosity (μ) is given by:

$$\mu(\dot{\gamma}) = \mu_\alpha + (\mu_0 - \mu_\alpha)\left(1 + K\mu^2\right)^{\frac{n-1}{2}} \tag{9}$$

where $\mu_a = 0.0345$ poise, $\mu_0 = 0.56$ poise, $K = 10.975$ s^2, and $n = 0.3568$.

Numerical strategy. A pressure–displacement mixed interpolation is used for the hexahedral solid elements to ensure incompressibility of the artery wall, while the fluid elements used a flow condition based interpolation (FCBI) scheme (Bathe and Zhang, 2002). Also, a 2nd order accurate trapezoidal time integration scheme with a time step size of 0.0025 s is used to compute the transient pressure-flow hemodynamics and artery deformation. All the numerical calculations for the BWI study are performed using the FE method (ADINA 9.3, ADINA R&D Inc.).

Determination of artery wall compliance. The compliance of the artery wall can be obtained numerically and experimentally using the simple expression:

$$c = \frac{A_{max} - A_{min}}{p_{max} - p_{min}} \tag{10}$$

where A_{max} and A_{min} are the maximum and minimum lumen cross-sectional areas ($A = \pi d^2/4$) over the pulse cycle, while p_{max} and p_{min} are the maximum and minimum trans-luminal pressures over the pulse cycle, respectively.

3. Results

Assessing the shape matching inverse algorithm for determining realistic pre-stress in the PA wall forms a major part of the result. First, the load-free and pre-stressed geometries have been evaluated to compare changes in arterial diameter and its wall thickness under the influence of the applied *in vivo* loads. The pre-stress levels in the PA wall have been presented next, followed by the evaluation of the hemodynamic pressure-flow results at the PC-MRI planes. These numerical results are compared with measurements of data obtained under clinical settings. Finally, the $p - d$ relationship for the MPA and LPA and the associated compliances have been compared with experimental data.

3.1. Evaluation of compliant arterial wall pre-stress

Load-free and pre-stressed PA geometries. Fig. 6(A) shows the load-free PA geometry obtained from the inverse algorithm. The 8-noded structured hexahedral mesh used for the PA geometry is also visible. Upon application of the *in vivo* δ_{IV} (from Table 1) and the *in vivo* P_{IV} on $A(x_{LF}, 0)$, the pre-stressed geometry [$A(x_{PS}, \sigma_{PS})$] is obtained. An overlaid view of the $A(x_{LF}, 0)$ and $A(x_{PS}, \sigma_{PS})$ PA geometries is shown in Fig. 6(B). $A(x_{PS}, \sigma_{PS})$ is represented by a lighter shade, while the $A(x_{LF}, 0)$ with a darker shade. The cut-section view of the overlaid geometries also indicates the locations of the PC-MRI planes.

From Fig. 6(B), the overlaid geometries show a distinct increase in thickness of the $A(x_{LF}, 0)$ compared to $A(x_{PS}, \sigma_{PS})$, which is a result of the incompressibility constraint on the PA wall. The centerline of the PA geometry is fixed, and $A(x_{LF}, 0)$ shows a reduction in the axial and radial directions compared to $A(x_{PS}, \sigma_{PS})$. In order to quantify these observations, the dimensions of the $A(x_{LF}, 0)$ and $A(x_{PS}, \sigma_{PS})$ are compared with the $A(x_{IV}, 0)$ and are reported in Table 2. The MPA shows a 28.2% $[(22.93 - 16.47)/22.93 \times 100]$ reduced inner diameter (ID), a 18.8% $[(28.05 - 22.76)/28.05 \times 100]$ reduced outer diameter (OD) and a 23% $[(3.15 - 2.56)/2.56 \times 100]$ increased thickness in $A(x_{LF}, 0)$ compared to $A(x_{IV}, 0)$. On a similar note, the LPA shows a 30.5% $[(18.09 - 12.57)/18.09 \times 100]$ reduced inner diameter (ID), a 20.4% $[(21.68 - 17.26)/21.68 \times 100]$ reduced outer diameter (OD) and a 30.9% $[(2.35 - 1.79)/1.79 \times 100]$ increased thickness in $A(x_{LF}, 0)$ compared to $A(x_{IV}, 0)$. Finally, The RPA displays a 24.8% $[(15.96 - 11.99)/15.96 \times 100]$ reduced inner diameter (ID), a 16.2% $[(19.93 - 16.70)/19.93 \times 100]$ reduced outer diameter (OD) and a 18.4% $[(2.35 - 1.99)/1.99 \times 100]$ increased thickness in $A(x_{LF}, 0)$ compared to $A(x_{IV}, 0)$.

Satisfaction of the objective function [$E = \max_N |x^i_{PS} - x_{IV}|$] of the inverse algorithm is an important indicator of the successful implementation of the technique. While the maximum nodal error (0.43 mm) is computed to be somewhat higher than the tolerance (0.1 mm), all the dimensions for $A(x_{PS}, \sigma_{PS})$ measured at the three PC-MRI planes are within 5% of the corresponding $A(x_{IV}, 0)$ dimensions (Table 2).

As the *in vivo* loads deform the PA geometry from $A(x_{LF}, 0)$ to $A(x_{PS}, \sigma_{PS})$, the wall pre-stress, σ_{PS} is generated to ensure the static equilibrium of the arterial wall with the *in vivo* loads. It is worth noting that the previously obtained artery properties and artery wall thickness information is required to obtain the σ_{PS} from the pressure and axial stretch loads. The results for the artery wall pre-stress including stress–strain contours are presented in the Appendix.

3.2. PA pressure-flow hemodynamics and compliance evaluation using BWI

Fluid-domain boundary conditions. Since the computational domain for the PA branch model extends beyond the PC-MRI measurement planes, implementation and comparison of the patient-specific fluid domain boundary conditions (BC's) is an important result of the study. The pressure and velocity BC's applied at the boundaries of the computational domain are iterated (as described in the Methods section) such that a close agreement is obtained between the corresponding experimental and numerical values at the PC-MRI measurement locations.

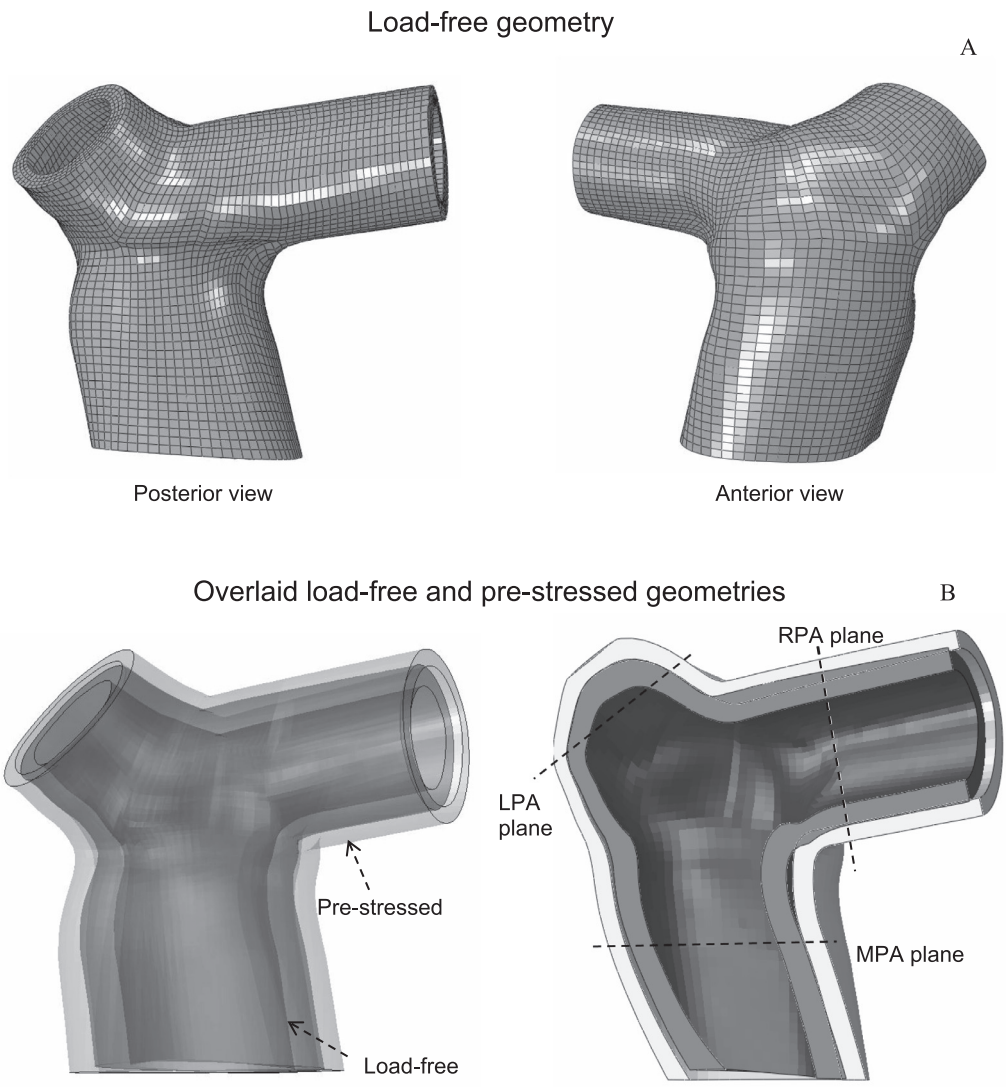

Fig. 6. (A) Load-free PA geometry obtained from the shape matching algorithm. (B) Load-free geometry overlaid with the pre-stressed geometry, with PC-MRI planes indicated.

Table 2
Comparison of the dimensions of load-free and pre-stressed geometries computed by the shape matching inverse algorithm with the *in vivo* geometry.

	Load-free (*LF*)	*In vivo* (*IV*)	$\% = \frac{IV-LF}{IV} \times 100$	Pre-stressed (*PS*)	$\% = \frac{IV-PS}{IV} \times 100$
MPA					
Inner diameter (mm)	16.47	22.93	28.2	23.56	−2.7
Outer diameter (mm)	22.76	28.05	18.8	28.46	−1.4
Thickness (mm)	3.15	2.56	−23.0	2.45	4.4
LPA					
Inner diameter (mm)	12.57	18.09	30.5	17.73	2.0
Outer diameter (mm)	17.26	21.68	20.4	21.35	1.5
Thickness (mm)	2.35	1.79	−30.9	1.81	−0.8
RPA					
Inner diameter (mm)	11.99	15.96	24.8	15.88	0.5
Outer diameter (mm)	16.70	19.93	16.2	19.80	0.6
Thickness (mm)	2.35	1.99	−18.4	1.96	1.2

Fig. 7(A) compares the pulsatile p_{LPA-e} measured at the LPA measurement plane with the numerical pressure profile (p_{LPA-n}) at the PC-MRI plane. Qualitatively close agreement of p_{LPA-e} and p_{LPA-n} is observed over the pulse cycle, confirming the successful implementation of the pressure BC used at the LPA computational boundary. The measured peak systolic p_{LPA-e} is 0.4% $[(22.4-22.3)/22.4 \times 100]$ higher than the corresponding computed p_{LPA-n} values, while the end diastolic p_{LPA-e} is nearly the same as the numerical value (12.0 mmHg).

Fig. 7(B) compares the flow-rates, Q_{MPA-e} and Q_{RPA-e}, measured at the respective PC-MRI planes with the corresponding numerical profiles: Q_{MPA-n} and Q_{RPA-n}. Again, qualitatively close agreement is

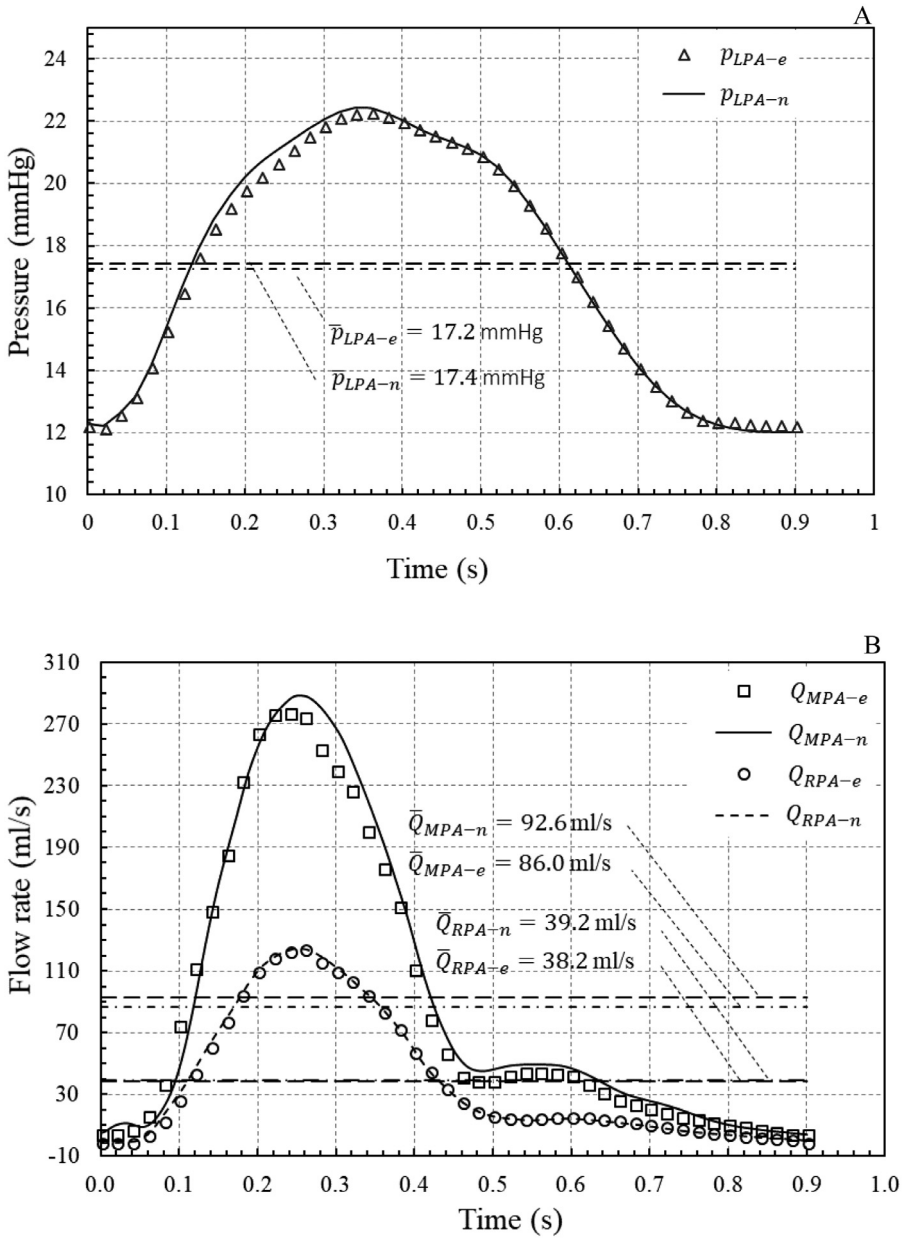

Fig. 7. (A) Comparison of experimental and numerical pressures at the PC-MRI plane of the LPA. (B) Comparison of experimental and numerical flow rates at the RPA and MPA measurement planes.

observed between the numerical and experimental values, verifying the successful implementation of the velocity BC's used at the computational boundaries of the MPA and RPA. The peak systolic Q_{MPA-e} value is 2.9% $[(285.6 - 277.3)/285.6 \times 100]$ lower than the corresponding Q_{MPA-n} value, while the peak diastolic Q_{MPA-e} value is 9.7% $[(49.4 - 44.6)/49.4 \times 100]$ lower than the corresponding numerical value. Further, the mean experimental MPA flow rate ($\bar{Q}_{MPA-e}$) is 6.2% $[(92.6 - 86.9)/92.6 \times 100]$ lower than the corresponding $\bar{Q}_{MPA-n}$.

On a similar note, the peak systolic Q_{RPA-e} is nearly the same as the corresponding Q_{RPA-n} value (124.4 ml/s). The peak diastolic Q_{RPA-e} value is 11.1% $[(16.0 - 14.4)/14.4 \times 100]$ higher than the corresponding numerical Q_{RPA-n} value. Also, the mean flow rate $\bar{Q}_{RPA-e}$ is found to be 2.6% $[(39.2 - 38.2)/38.2 \times 100]$ higher than the corresponding $\bar{Q}_{RPA-n}$.

Comparison of experimental and numerical pressure-flow hemodynamics. Comparing numerical measures of the pressure-flow hemodynamics of the compliant PA branch with patient-specific data is one of the primary outcomes of this study. The comparison between the transient p_{MPA-e} and the p_{MPA-n} profiles is shown in Fig. 8(A). Although there is some difference between the profiles, particularly at peak systole, reasonable agreement is observed over the pulse cycle. The peak systolic p_{MPA-e} measured at 0.3 s is 9.7% $[(23.6 - 21.3)/23.6 \times 100]$ lower than the corresponding numerical p_{MPA-n}. The peak diastolic p_{MPA-e} measured just after the dicrotic notch at 0.5 s is 3.8% $[(21.2 - .4)/21.2 \times 100]$ lower than the corresponding numerical value. Further, the time-averaged pressure $\bar{p}_{MPA-e}$ is measured to be 3.4% $[(17.8 - 17.2)/17.8 \times 100]$ lower than the corresponding $\bar{p}_{MPA-n}$ value at the MPA measurement plane. The numerical results for p_{MPA-n} are also compared with the refined fluid mesh (Fig. 8(A)). The p_{MPA-n} profile for the baseline (coarse) mesh agreed qualitatively well with the profile for the refined mesh. All values of the pressure profile for the refined mesh are within 10% of the values for the baseline mesh.

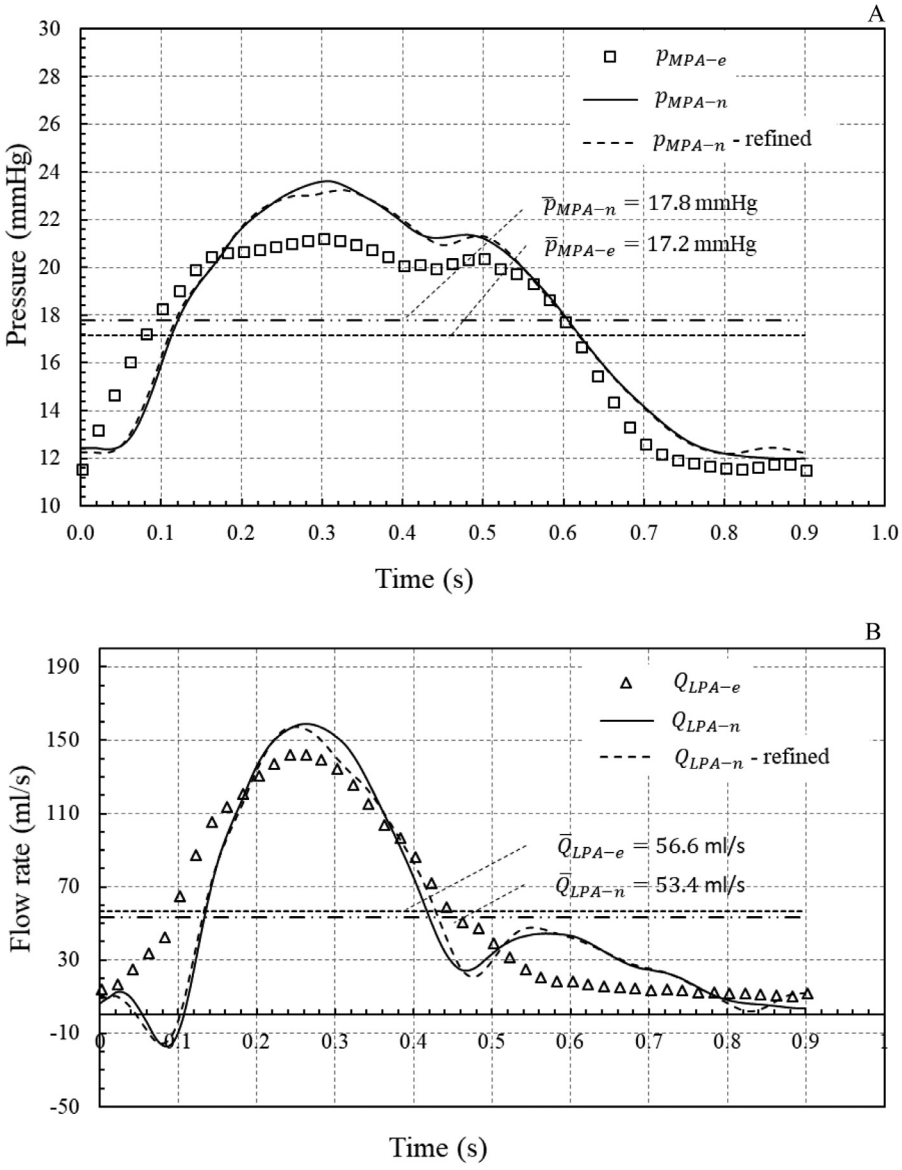

Fig. 8. (A) Comparison of experimental and numerical pressures at the MPA measurement plane. (B) Comparison of experimental and numerical flow rates at the LPA measurement plane.

A similar comparison has been performed between the measured Q_{LPA-e} and the computed Q_{LPA-n} (Fig. 8(B)), both quantities evaluated at the PC-MRI plane of the LPA. Although there are some differences in the transient Q profiles, particularly in the early systole and the diastolic region of the pulse cycle, reasonable agreement is observed between these quantities. The peak systolic Q_{LPA-e} value at 0.26 s is measured to be 10% $[(158.9 - 143.0)/158.9 \times 100]$ lower than the computed peak systolic Q_{LPA-n} value. The time-averaged flow rate $\bar{Q}_{LPA-e}$ is measured to be 6% $[(56.6 - 53.4)/53.4 \times 100]$ higher than the $\bar{Q}_{LPA-n}$ value computed at the LPA measurement plane. Again, the Q_{LPA-n} profile for baseline mesh is compared with the refined mesh. Similar to the p_{MPA-n}, all values of the flow rate profile for the refined mesh are within 10% of the values for the baseline mesh.

Comparison of experimental and numerical pressure–diameter variation with time. Pressure–diameter variation with time provides valuable insight into the importance of the selected patient-specific material model and its influence on compliance. Fig. 9(A) shows the comparison between p_{MPA-e} and p_{MPA-n}, and between the experimental lumen diameter (d_{MPA-e}) and numerical lumen diameter (d_{MPA-n}). Reasonable agreement is observed between the quantities over the pulse cycle. The peak systolic d_{MPA-n} computed at 0.28 s is noted to be 3.6% $[(26.86 - 26.51)/26.51 \times 100]$ lower than the corresponding d_{MPA-e} measured at 0.34 s. Further, the time-averaged numerical diameter ($\bar{d}_{MPA-n}$) is computed to be within 0.1% $[(23.30 - 23.28)/23.30 \times 100]$ of the $\bar{d}_{MPA-e}$ value.

On a similar note for the LPA, Fig. 9(B) shows the comparisons between p_{LPA-e} and p_{LPA-n}, as well as between d_{LPA-e} and the numerical d_{LPA-n} measured at the LPA measurement plane. Again, the experimental and numerical quantities show similar profiles over the pulse cycle. The numerical peak systolic d_{LPA-n} value computed at 0.32 s is found to be 1.4% $[(18.66 - 18.40)/18.66 \times 100]$ lower than the corresponding d_{LPA-e} measured at 0.38 s. Further, the time-averaged experimental diameter $\bar{d}_{LPA-e}$ is computed to be 0.2% $[(17.56 - 17.52)/17.56 \times 100]$ lower than the corresponding $\bar{d}_{LPA-n}$ value.

Comparison of experimental and numerical pressure–diameter relationships. Here, a previously developed non-linear least squares optimization technique is used to derive artery-specific material models from patient-specific $p - d$ relationships. One of the

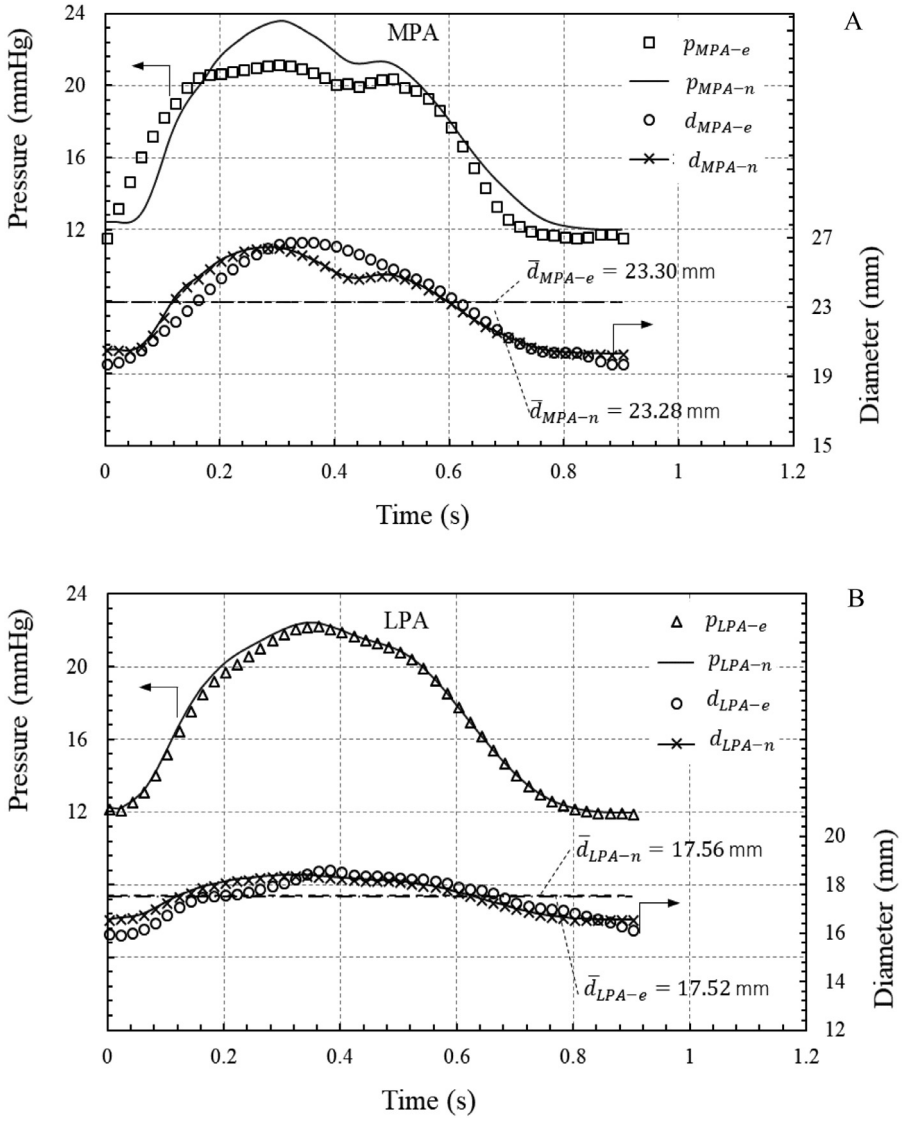

Fig. 9. (A) Comparison of experimental and numerically computed pressures and diameters at the MPA measurement plane. (B) Comparison of experimental and numerically computed pressures and diameters at the LPA measurement plane.

outcomes of this numerical study is to assess the material models using a BWI computation and obtain measures for compliance of the PA walls. Fig. 10 plots pressure versus the lumen diameter of the MPA and LPA. The results from the numerical calculation agree reasonably well with the experimental values. The experimental $p-d$ relationships for the MPA and LPA enclose a non-zero volume, a possible outcome of existence of arterial wall viscoelasticity or due to the pressure and diameter measurements being done at different, but nearby locations. In contrast, the numerical $p-d$ relationships do not exhibit this feature as the material model does not account for wall viscoelasticity, while the numerical $p-d$ data are obtained at the PC-MRI plane locations.

The numerical compliance (c_{LPA-n}) of the LPA is calculated to be 5.51 mm^2/mmHg, which is found to be 20.3% [$(6.92-5.51)/6.92\times 100$] lower than c_{LPA-e}. Similarly, the numerical c_{MPA-n} is calculated to be 19.56 mm^2/mmHg, which is 27% [$(26.79-19.56)/26.79\times 100$] lower than c_{MPA-e}. Importantly, the LPA shows significantly lower overall compliance compared to the MPA for both the numerical calculations and the experimental data. From the experimental $p-d$ data, c_{MPA-e} is measured to be 3.9 times the c_{LPA-e}. On a similar note, the c_{MPA-n} is computed to be 3.6 times the c_{LPA-n} in the numerical results.

4. Discussion

Artery-specific material properties. In this study, artery-specific properties are obtained using a non-linear least squares optimization technique developed by D'Souza et al. (2017). It is reported in literature that the material response of arteries is generally anisotropic (Fung et al., 1979; Holzapfel et al., 2000; Weizsacker and Pinto, 1988; Ogden, 2003), implying different properties in the circumferential, radial and longitudinal directions. In order to avoid the large number of constitutive model constants involved in a fully anisotropic model, Holzapfel et al. (2000) first modeled the artery as a layered fiber-reinforced material with the collagenous component acting as fibers, thus rendering the artery orthotropic in each layer. In the Mooney–Rivlin SEP chosen for this study, the third term in Eq. (1) with constants k_1 and k_2 represents the collagenous fibers assumed to be oriented along the circumferential

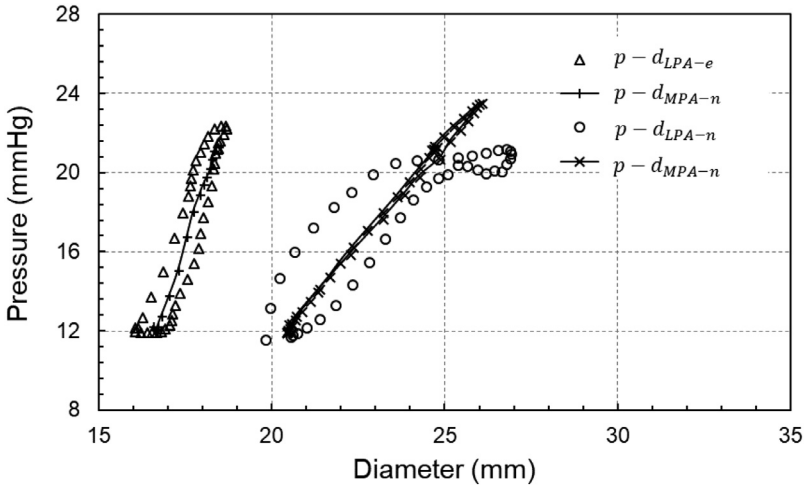

Fig. 10. Comparison of experimental and numerical pressure–diameter relationships for the MPA and LPA.

direction. Referring to Table 1, the optimization procedure results in the MPA showing nearly isotropic behavior, while the stiffer orthotropic LPA material shows non-zero values for k_1 and k_2. Further, the thin-walled cylinder assumption used in developing the material models has also been reported to be reasonable for problems involving bending, inflation and axial extension, while neglecting torsional deformation (Hunter et al., 2011). Also, all wall stresses including residual pre-stress are included since the material properties in this research are developed from the experimental $p-d$ relationships,

In the course of developing the MPA material model, the considered $p-d$ relationship is limited to a maximum d value of 25 mm. Previous studies have shown that healthy PA walls show stiffening behavior at higher pressures due to the engagement of collagen fibers (Hunter et al., 2011; Tian et al., 2016). For this study, the non-physiological softening response observed in the $(p-d)_{MPA-e}$ (Fig. 2(A)) beyond 25 mm could be the result of p and d measurements not being performed at the same location. Further, it is known that the softening of the arterial wall at higher $p-d$ values could lead to numerical instability in the BWI calculation. This is because the stiffness of the MPA reduces incorrectly in the presence of unrealistic expansion (increased diameter) of the artery under the applied transmural pressure.

From Table 2, the δ_{IV}'s computed for the MPA (3%) and LPA (4%) as best-fit parameters from the non-linear least squares calculation are somewhat lower than the axial stretches of 1.1 to 1.47 observed for other arteries in literature (Huang et al., 2009; Tang et al., 2004). Lower axial stretches are considered reasonable for PAs because they are exposed to lower pressures (10–20 mmHg) compared to the carotid or coronary artery pressure (80–120 mmHg). Furthermore, the computed δ_{IV}'s agree well with the axial pre-stretch of 1.025 to 1.05 reported by Chesler et al. (2004) in their experimental study of mouse pulmonary artery biomechanics, while recognizing the higher stretch ratios of 1.4 to 1.7 suggested by Huang et al. (2001a,b) for rat pulmonary arterial segments and 1.15 to 1.3 suggested by Debes et al. (1995) for canine pulmonary arteries. It may be noted that the existing literature does not report stretch ratios for human PA's, which is the focus of this study.

Shape matching inverse algorithm. The current shape matching inverse algorithm improves upon the previous algorithms proposed by Das et al. (2015a,b) and Banerjee et al. (2017) which have used idealized straight and tapered artery geometries. This study has used a patient-specific pulmonary artery branch with *non-circular geometry* and *variable thickness*. It may be noted that the *in vivo* δ_{IV} is assumed to be fixed over the course of the forward FE computation in the F operator for the three artery branches, while it is reported that the axial stretch changes *in vivo* with the dynamic transmural lumen pressure (Zhang et al., 2005; Wang and Chesler, 2012). A backward displacement approach proposed by Bols et al. (2013) is implemented in the S operator to obtain the load-free geometry $[A(x_{LF}, 0)]$ from the stress-free $A(x_{IV}, 0)$, compared to the optimization based algorithms used in literature (Raghavan et al., 2006; Das et al., 2015a,b; Banerjee et al., 2017; Lu et al., 2008). This allows for a simple, but robust algorithm that iteratively updates the nodal positions without a costly optimization routine, while including physiological features such as artery-specific material properties and incompressibility in the forward FE calculation. Recently, Mousavi et al. (2017) have also proposed an iterative algorithm where the elastin deformation gradient computed for the current configuration from the reference configuration is used as the next guess for the stretch deposition tensor. This is in contrast to the backward displacement technique used in this study which relies only on nodal positions, with no computation of gradients. The inverse algorithm's objective function ($x_{PS} = x_{IV}$) is satisfied with a maximum nodal error of 0.43 mm in 13 iterations to yield the $A(x_{LF}, 0)$ and the σ_{PS}. While it is impossible to experimentally obtain patient-specific load-free arterial geometries, the accuracy of the computed $A(x_{LF}, 0)$ can be deduced by comparing/assessing the wall pre-stress, arterial wall shrinkage and more importantly, compliance values of the stressed artery $A(x_{PS}, \sigma_{PS})$ under pulsatile hemodynamics.

Load-free PA geometry. The orthotropic Mooney–Rivlin SEP used in this study, along with the *in vivo* δ_{IV} and the incompressibility constraint has resulted in a distinctly thicker arterial wall and axially shrunk artery $A(x_{LF}, 0)$. The MPA, LPA and RPA show a mean inner diameter (ID) shrinkage of 27.9% from the $A(x_{PS}, \sigma_{PS})$. This lies within the range of ID shrinkages that varies from 18% to 33% (Hamza et al., 2003) for the left anterior descending coronary artery of pigs at 0 mmHg transmural pressure. On the other hand, Huang et al. (2009) have used *in vivo* and *ex vivo* MRI images to report an ID shrinkage of 7.9% for the human carotid artery. However, it is to be noted that the carotid artery is stiffer and displays significantly higher transmural pressure compared to the pulmonary arteries. Previous studies by our group have also reported 14% ID shrinkage for an idealized cylindrical artery (Das et al., 2015a,b), and 18–20% ID shrinkage for the tapered canine femoral artery (Banerjee et al., 2017). The ID shrinkages reported in this study generally agree with the values reported in literature, strengthening the validity of the $A(x_{LF}, 0)$ used in the study.

In the loaded *in vivo* state, the PA walls generate an average pre-stress in order to maintain equilibrium with the applied *in vivo* pressure P_{IV} and axial stretch, δ_{IV}. The pre-stress observed in this study generally agrees with values reported in literature and further discussion is presented in the Appendix.

PA pressure-flow hemodynamics. Obtaining physiologic values of pressure-flow relationship of the PA branch is an important outcome of this study as it strengthens the numerical technique's potential as a predictive tool for pre-surgical evaluation. Hemodynamic quantities such as wall shear stress (WSS) are important indicators of plaque formation in arteries as reported by several studies (Wentzel et al., 2012; Dhawan et al., 2010; Thim et al., 2012). Our previous studies have also proposed hemodynamic and energy-based endpoints which evaluate the health of the right ventricle and the pulmonary vasculature (Das et al., 2011, 2015a,b). Since the current study is performed on healthy pulmonary vasculature with limited clinical measurements, the hemodynamic analysis is limited to assessing and comparing the p and Q profiles for a healthy subject. Fig. 8(A) shows a reasonable agreement between p_{MPA-n} and p_{MPA-e}. Importantly, p_{MPA-n} shows a distinct dicrotic notch, a physiological feature which represents the closing of the pulmonary valve. Although, there is a difference in peak systolic p values, the numerical waveform resembles profiles reported by other studies for normal pulmonary vasculature (Nakayama et al., 1997; Singal et al., 2015), where the peak systolic p is higher than the peak diastolic p measured after the dicrotic notch. Fig. 8(B) again shows a reasonable agreement between the Q_{LPA-e} and Q_{LPA-n}. There is a difference in the early systolic part of the Q profiles where the numerical waveform shows reverse flow. This could be the result of known lower accuracy of measured PC-MRI data near the arterial wall and reduced flow regions. However, it must be noted that mean values for both p_{MPA-n} and Q_{LPA-e} show close agreement with the corresponding experimental values, adding credence to the current methodology.

Variable PA wall compliance. Arterial wall composition and microstructure is known to be highly heterogenous, and wall properties are known to vary between different arteries, and their measurement locations (Fung et al., 1979). Including these variations in the numerical BWI calculations can lead to more accurate measures of hemodynamics, and arterial compliance and wall stress. Our previous study (D'Souza et al., 2017) has delineated the wall properties of the main and branched PA's, accounting for both intra-vessel variability and inter-subject variabilities. For example, Fig. 9 shows the difference in the transient $p-d$ relationship between the MPA and LPA. The diameter variation for the LPA over the pulse cycle is significantly lesser than the MPA for similar pressure variation, suggesting lower compliance for the LPA. This is confirmed in Fig. 10, where the $(p-d)_{LPA}$ slope is higher compared to the $(p-d)_{MPA}$. Further, the numerical c values show about four-fold increase in MPA compliance compared to the LPA. Failing to account for such intra-vessel variations in 3D numerical BWI calculations can lead to inaccurate measures for pressure-flow hemodynamics and consequently artery wall compliance.

Limitations and future directions. Although the current study successfully computed pressure-flow hemodynamics as well as compliance for a 3D patient-specific artery geometry with artery-specific material properties, there are a few limitations. Considering this is a retrospective study on data obtained from a single patient, the pressure and diameter measurements are not necessarily made exactly at the same location, possibly leading to the relatively higher hysteresis of the $p-d$ relationship for the MPA. Also, *in vivo* p measurements have not been conducted for the RPA, thus artery-specific material properties for the RPA could not be implemented. Further, the PC-MRI measurements have not been conducted at the boundary of the computational domain, thus requiring an iterative procedure to compute and extrapolate the patient-specific BC's Finally, the current procedure relied on invasive catheterization measurements for p profiles; however non-invasive modalities such as 4D MRI measurements can be used for obtaining pressure-flow data, as demonstrated by Campobasso et al. (2018) in their recent BWI study on the ascending aorta. Most of the limitations in the study can be addressed by a future prospective clinical trial with a complete set of hemodynamics measurements under clinical settings.

In summary, the current study has been conceived as a proof of concept to obtain patient-specific load-free and pre-stressed artery geometries, with compliance obtained from a BWI calculation with patient-specific boundary conditions. However, refinements to the computational model are required for further evaluation of hemodynamic markers. In future, the technique proposed in this study can assist in improving hemodynamic and energy endpoints for longitudinal assessment of vasculatures.

5. Conclusion

In this numerical study, the inverse algorithm has been successfully implemented for a 3D patient-specific PA geometry with artery-specific wall properties for the MPA and LPA to obtain the load-free and pre-stressed geometries. The load-free PA geometry shows a 27.8% lower inner d and a 18.5% lower outer d compared to the *in vivo* geometry. From the BWI computation performed with the load-free PA geometry, the mean p_{MPA-e} is observed to be 3.4% lower than the corresponding p_{MPA-n}. Similarly, the mean Q_{LPA-e} is measured to be 10% lower than the mean Q_{LPA-n}. Further, the PA wall compliance has been computed from the numerical $p-d$ relationship and compared with the experimental compliance. The c_{LPA-n} is computed to be 5.51 mm^2/Hg which is 20.3% lower than c_{LPA-e} (6.92 mm^2/mmHg), while c_{MPA-n} is computed to be 19.56 mm^2/Hg which is 27% lower than c_{MPA-e}. The PA wall shows significant intra-vessel variability with the MPA showing significantly higher overall compliance compared to the LPA (3.5–4 times) in the numerical computations as well as the experimental measurements. In summary, numerical calculations of BWI in patient-specific PA geometries with wall pre-stress can be utilized for the evaluation of healthy or diseased pulmonary vasculature and aid the diagnosis of vascular disease

Conflict of interest

None.

Appendix

Fig. A1(A) shows a von Mises stress contour overlaid on the geometry defined by $A(x_{PS}, \sigma_{PS})$. Since the *in vivo* pressure acts on the inner surface of the PA wall, the stresses reduce from the inner fibers to the outer fibers of the artery wall. The stress values vary from 20–30 kPa at the inner surface to values of 5–10 kPa near the outer surface of the artery wall. Fig. A1 also shows the maximum principal log-strain contour overlaid on $A(x_{PS}, \sigma_{PS})$. The strains generated due to the *in vivo* loads follow a similar trend as the stresses; inner fibers show higher strain values compared to the outer fibers. The values vary from 0.15 to 0.25 at the outer fibers to higher values of 0.3–0.5 at the inner fibers. It may be noted that the MPA wall shows relatively higher values of strain compared to the LPA and RPA.

The PA wall pre-stress values in this study range from 5 to 30 kPa. Although there are limited studies on wall pre-stress values for human pulmonary arteries, Teeter et al. (2010) have used FE computations to compute wall stress in horse pulmonary arteries. Wall stress values of 10–70 kPa have been reported at 25 mmHg, which is close to the P_{IV} of 17.2 mmHg used and stresses

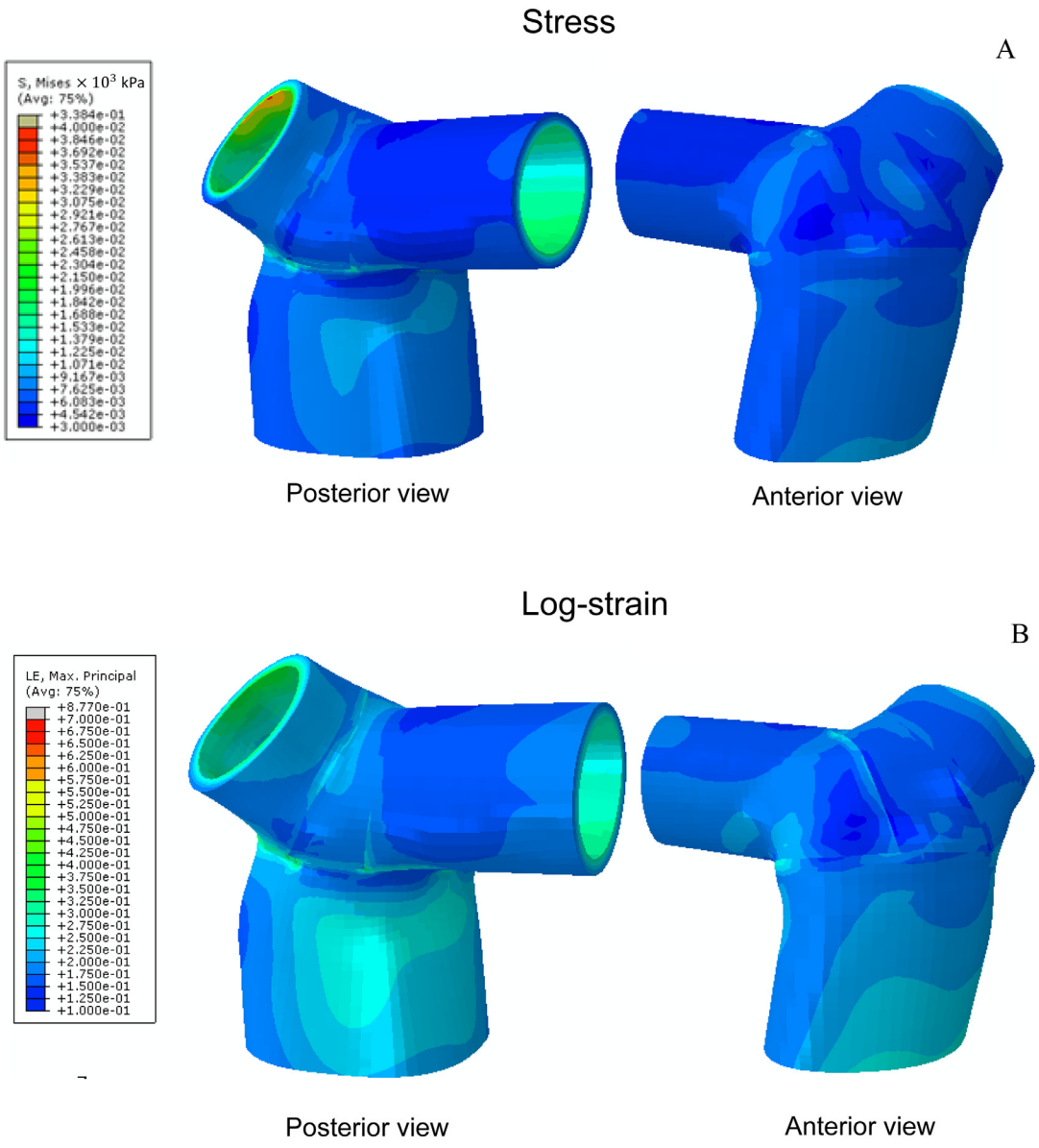

Fig. A1. (A) Pre-stressed shape overlaid with a von Mises stress contour (B) Pre-stressed PA shape overlaid with a principal log-strain contour.

(Fig. A1(B)) obtained in this study. FE calculations performed on human carotid arteries by Tao et al. (2015) has reported maximum pre-stress values of 35 kPa which are close to the values observed in the current study, although higher transmural pressures of 80–120 mmHg are observed in the carotid arteries compared to values of 10–20 mmHg in the pulmonary arteries. In summary, the pre-stress levels in this study generally follow the values reported in literature, further strengthening the validity of the inverse algorithm formulation as well as the A(x_{LF}, 0) used in this computational research.

References

Banerjee, R.K., D'Souza, G.A., Paul, A.K., Das, A., 2017. Evaluation of hemodynamics in a prestressed and compliant tapered femoral artery using an optimization-based inverse algorithm. J. Biomech. Eng. 139 (4), 041002.

Bathe, K.J., Zhang, H., 2002. A flow-condition-based interpolation finite element procedure for incompressible fluid flows. Comput. Struct. 80 (14–15), 1267–1277.

Bathe, K.J., Zhang, H., 2009. A mesh adaptivity procedure for CFD and fluid-structure interactions. Comput. Struct. 87 (11–12), 604–617.

Bogren, H.G., Klipstein, R.H., Mohiaddin, R.H., Firmin, D.N., Underwood, S.R., Rees, R.S., Longmore, D.B., 1989. Pulmonary artery distensibility and blood flow patterns: a magnetic resonance study of normal subjects and of patients with pulmonary arterial hypertension. Am. Heart J. 118 (5 Pt 1), 990–999.

Bols, J., Degroote, J., Trachet, B., Verhegghe, B., Segers, P., Vierendeels, J., 2013. A computational method to assess the in vivo stresses and unloaded configuration of patient-specific blood vessels. J. Comput. Appl. Math. 246, 10–17.

Borges, A.C., Wensel, R., Opitz, C., Bauer, U., Baumann, G., Kleber, F.X., 1997. Relationship between haemodynamics and morphology in pulmonary hypertension. A quantitative intravascular ultrasound study. Eur. Heart J. 18 (12), 1988–1994.

Campobasso, R., Condemi, F., Viallon, M., Croisille, P., Campisi, S., Avril, S., 2018. Evaluation of peak wall stress in an ascending thoracic aortic aneurysm using FSI simulations: effects of aortic stiffness and peripheral resistance. Cardiovasc. Eng. Technol. 9 (4), 707–722.

Canepa, A., Chavez, R., Hurtado, A., Rotta, A, Velasquez, T., 1956. Pulmonary circulation at sea level and at high altitudes. J. Appl. Physiol. 9 (3), 328–336.

Chesler, N.C., Thompson-Figueroa, J., Millburne, K., 2004. Measurements of mouse pulmonary artery biomechanics. J. Biomech. Eng. 126 (2), 309–314.

Crosswhite, P., Sun, Z., 2014. Molecular mechanisms of pulmonary arterial remodeling. Mol. Med. 20, 191–201.

Das, A., Gottliebson, W.M., Karve, M., Banerjee, R., 2011. Comparison of hemodynamic endpoints between normal subject and tetralogy patient using Womersley velocity profile and MR based flow measurements. Mol. Cell Biomech. 8 (1), 21–42.

Das, A., Paul, A., Taylor, M.D., Banerjee, R.K., 2015a. Pulsatile arterial wall-blood flow interaction with wall pre-stress computed using an inverse algorithm. Biomed. Eng. Online 14 (Suppl 1), S18.

Das, A., Wansapura, J.P., Gottliebson, W.M., Banerjee, R.K., 2015b. Methodology for implementing patient-specific spatial boundary condition during a cardiac cycle from phase-contrast MRI for hemodynamic assessment. Med. Image Anal. 19 (1), 121–136.
de Putter, S., Wolters, B.J., Rutten, M.C., Breeuwer, M., Gerritsen, F.A., van de Vosse, F.N., 2007. Patient-specific initial wall stress in abdominal aortic aneurysms with a backward incremental method. J. Biomech. 40 (5), 1081–1090.
Debes, J.C., Fung, Y.C., 1995. Biaxial mechanics of excised canine pulmonary arteries. Am. J. Physiol. 269 (2 Pt 2), H433–H442.
Dhawan, S.S., Avati Nanjundappa, R.P., Branch, J.R., Taylor, W.R., Quyyumi, A.A., Jo, H., McDaniel, M.C., Suo, J., Giddens, D., Samady, H., 2010. Shear stress and plaque development. Expert Rev. Cardiovasc. Ther. 8 (4), 545–556.
D'Souza, G.A., Taylor, M.D., Banerjee, R.K., 2017. Evaluation of pulmonary artery wall properties in congenital heart disease patients using cardiac magnetic resonance. Prog. Pediatric Cardiol. 47, 49–57.
Fung, Y.C., Fronek, K., Patitucci, P., 1979. Pseudoelasticity of arteries and the choice of its mathematical expression. Am. J. Physiol. 237 (5), H620–H631.
Gee, M.W., Reeps, C., Eckstein, H.H., Wall, W.A., 2009. Prestressing in finite deformation abdominal aortic aneurysm simulation. J. Biomech. 42 (11), 1732–1739.
Govindjee, S., Mihalic, P.A., 1996. Computational methods for inverse finite elastostatics. Comput. Methods Appl. Mech. Eng. 136 (1–2), 47–57.
Hamza, L.H., Dang, Q., Lu, X., Mian, A., Molloi, S., Kassab, G.S., 2003. Effect of passive myocardium on the compliance of porcine coronary arteries. Am. J. Physiol. Heart Circ. Physiol. 285 (2), H653–H660.
Holzapfel, G.A., Ogden, R.W., 2014. Biomechanics of Soft Tissue in Cardiovascular Systems. Springer Vienna.
Holzapfel, G.A., Gasser, T.C., Ogden, R.W., 2000. A new constitutive framework for arterial wall mechanics and a comparative study of material models. J. Elast. 61 (1–3), 1–48.
Huang, W., Delgado-West, D., Wu, J.T., Fung, Y.C., 2001a. Tissue remodeling of rat pulmonary artery in hypoxic breathing. II. Course of change of mechanical properties. Ann. Biomed. Eng. 29 (7), 552–562.
Huang, W., Sher, Y.P., Delgado-West, D., Wu, J.T., Peck, K., Fung, Y.C., 2001b. Tissue remodeling of rat pulmonary artery in hypoxic breathing. I. Changes of morphology, zero-stress state, and gene expression. Ann. Biomed. Eng. 29 (7), 535–551.
Huang, X., Yang, C., Yuan, C., Liu, F., Canton, G., Zheng, J., Woodard, P.K., Sicard, G.A., Tang, D., 2009. Patient-specific artery shrinkage and 3D zero-stress state in multi-component 3D FSI models for carotid atherosclerotic plaques based on in vivo MRI data. Mol. Cell Biomech. 6 (2), 121–134.
Hunter, K.S., Lammers, S.R., Shandas, R., 2011. Pulmonary vascular stiffness: measurement, modeling, and implications in normal and hypertensive pulmonary circulations. Compr. Physiol. 1 (3), 1413–1435.
Hunter, K.S., Lanning, C.J., Chen, S.Y.J., Zhang, Y.H., Garg, R., Ivy, D.D., Shandas, R., 2006. Simulations of congenital septal defect closure and reactivity testing in patient-specific models of the pediatric pulmonary vasculature: a 3D numerical study with fluid-structure interaction. J. Biomech. Eng.-Trans. ASME 128 (4), 564–572.
Jin, S., Oshinski, J., Giddens, D.P., 2003. Effects of wall motion and compliance on flow patterns in the ascending aorta. J. Biomech. Eng. 125 (3), 347–354.
Konala, B.C., Das, A., Banerjee, R.K., 2011. Influence of arterial wall-stenosis compliance on the coronary diagnostic parameters. J. Biomech. 44 (5), 842–847.
Long, C.C., Hsu, M.C., Bazilevs, Y., Fenstein, J.A., Marsden, A.L., 2012. Fluid-structure interaction simulations of the Fontan procedure using variable wall properties. Int. J. Numer. Method Biomed. Eng. 28 (5), 513–527.
Lu, J., Zhou, X., Raghavan, M.L., 2008. Inverse method of stress analysis for cerebral aneurysms. Biomech. Model. Mechanobiol. 7 (6), 477–486.
Lu, J., Zhou, X.L., Raghavan, M.L., 2007. Computational method of inverse elastostatics for anisotropic hyperelastic solids. Int. J. Numer. Methods Eng. 69 (6), 1239–1261.
Megerman, J., Hasson, J.E., Warnock, D.F., L'Italien, G.J., Abbott, W.M., 1986. Noninvasive measurements of nonlinear arterial elasticity. Am. J. Physiol. 250 (2 Pt 2), H181–H188.
Mousavi, S.J., Avril, S., 2017. Patient-specific stress analyses in the ascending thoracic aorta using a finite-element implementation of the constrained mixture theory. Biomech. Model. Mechanobiol. 16 (5), 1765–1777.
Nakayama, Y., Nakanishi, N., Sugimachi, M., Takaki, H., Kyotani, S., Satoh, T., Okano, Y., Kunieda, T., Sunagawa, K., 1997. Characteristics of pulmonary artery pressure waveform for differential diagnosis of chronic pulmonary thromboembolism and primary pulmonary hypertension. J. Am. Coll. Cardiol. 29 (6), 1311–1316.
Ogden, R.W., 2003. Nonlinear elasticity, anisotropy, material stability and residual stresses in soft tissue. Biomech. Soft Tissue Cardiovasc. Syst. (441) 65–108.
Raghavan, M.L., Ma, B., Fillinger, M.F., 2006. Non-invasive determination of zero–pressure geometry of arterial aneurysms. Ann. Biomed. Eng. 34 (9), 1414–1419.
Roy, A.S., Back, L.H., Banerjee, R.K., 2008. Evaluation of compliance of arterial vessel using coupled fluid structure interaction analysis. MCB Mol. Cell. Biomech. 5 (4), 229–246.
Shimoda, L.A., Laurie, S.S, 2013. Vascular remodeling in pulmonary hypertension. J. Mol. Med. 91 (3), 297–309.
Singal, A., Gandhi, S., Pritzker, M., Thenappan, T., 2015. Methodologies for pulmonary artery pressure waveform and wave reflection analysis in patients with pulmonary hypertension. J. Med. Devices-Trans. ASME 9 (2).
Tang, D., Yang, C., Zheng, J., Woodard, P.K., Saffitz, J.E., Sicard, G.A., Pilgram, T.K., Yuan, C., 2005. Quantifying effects of plaque structure and material properties on stress distributions in human atherosclerotic plaques using 3D FSI models. J. Biomech. Eng. 127 (7), 1185–1194.
Tang, D., Yang, C., Zheng, J., Woodard, P.K., Sicard, G.A., Saffitz, J.E., Yuan, C., 2004. 3D MRI-based multicomponent FSI models for atherosclerotic plaques. Ann. Biomed. Eng. 32 (7), 947–960.
Tao, X., Gao, P., Jing, L., Lin, Y., Sui, B., 2015. Subject-Specific fully-coupled and one-way fluid-structure interaction models for modeling of carotid atherosclerotic plaques in humans. Med. Sci. Monit. 21, 3279–3290.
Teeter, M.G., Arroyo, L.G., Bakker, J.D., Hayes, M.A., Viel, L., Runciman, R.J., 2010. Finite element analysis of wall stress in the equine pulmonary artery. Equine Vet. J. 42 (1), 68–72.
Thim, T., Hagensen, M.K., Horlyck, A., Kim, W.Y., Niemann, A.K., Thrysoe, S.A., Drouet, L., Passke, W.P., Botker, H.E., Falk, E., 2012. Wall shear stress and local plaque development in stenosed carotid arteries of hypercholesterolemic minipigs. J. Cardiovasc. Dis. Res. 3 (2), 76–83.
Tian, L., Wang, Z.J., Liu, Y.M., Eickhoff, J.C., Eliceiri, K.W., Chesler, N.C., 2016. Validation of an arterial constitutive model accounting for collagen content and crosslinking. Acta Biomater. 31, 276–287.
Vavourakis, V., Hipwell, J.H., Hawkes, D.J., 2016. An inverse finite element u/p-formulation to predict the unloaded state of in vivo biological soft tissues. Ann. Biomed. Eng. 44 (1), 187–201.
Wang, Z., Chesler, N.C., 2012. Role of collagen content and cross-linking in large pulmonary arterial stiffening after chronic hypoxia. Biomech. Model. Mechanobiol. 11 (1–2), 279–289.
Weizsacker, H.W., Pinto, J.G., 1988. Isotropy and anisotropy of the arterial wall. J. Biomech. 21 (6), 477–487.
Wentzel, J.J., Chatzizisis, Y.S., Gijsen, F.J., Giannoglou, G.D., Feldman, C.L., Stone, P.H., 2012. Endothelial shear stress in the evolution of coronary atherosclerotic plaque and vascular remodelling: current understanding and remaining questions. Cardiovasc. Res. 96 (2), 234–243.
Zhang, Y., Dunn, M.L., Drexler, E.S., McCowan, C.N., Slifka, A.J., Ivy, D.D., Shandas, R., 2005. A microstructural hyperelastic model of pulmonary arteries under normo- and hypertensive conditions. Ann. Biomed. Eng. 33 (8), 1042–1052.

Ullhas Hebbar received his MS degree in Mechanical and Materials Engineering from the University of Cincinnati in 2018. This research is an excerpt of his MS Thesis. Currently he is a graduate student pursuing his PhD in Mechanical Engineering at Rensselaer Polytechnic Institute. Having obtained his Bachelor's degree in 2013 from the National Institute of Technology, Surathkal, India, Ullhas worked in the automotive industry at Bajaj Auto Ltd., India.

Rupak Banerjee is a Professor of Mechanical and Biomedical Engineering at the University of Cincinnati. As a faculty member since 2002, his research has focused on experimental study with analytical and numerical analysis involving transient physiologic and patho-physiologic flow, heat and mass transfer problems. After his PhD studies at Drexel University in 1992, he worked at Raytheon, Fluent Inc., the NIH and at Kettering University as an Assistant Professor. He has a publication record of more than 125 journal articles. Dr. Banerjee is also a Fellow of both ASME and AHA.